Journal of Alloys and Compounds 509 (2011) 7611–7617

Contents lists available at ScienceDirect

Journal of Alloys and Compounds

journal homepage: www.elsevier.com/locate/jallcom

Improvement in the low-temperature performance of AB_5 metal hydride alloys by Fe-addition

K. Young*, T. Ouchi, B. Reichman, J. Koch, M.A. Fetcenko

Energy Conversion Devices Inc./Ovonic Battery Company, 2983 Waterview Drive, Rochester Hills, MI 48309, USA

ARTICLE INFO

Article history:
Received 10 March 2011
Received in revised form 18 April 2011
Accepted 19 April 2011
Available online 27 April 2011

Keywords:
Hydrogen absorbing materials
Transition metal alloys
Metal hydride electrode
Electrochemical reactions

ABSTRACT

The structures and electrochemical properties of a series of annealed AB_5, $La_{10.5}Ce_{4.3}Pr_{0.5}Nd_{1.4}Ni_{64.3-x}Co_{5.0}Mn_{4.6}Al_{6.0}Cu_{3.2}Zr_{0.2}Fe_x$ ($x = 0.0$, 0.5, 1.0, and 1.5), metal hydride alloys were studied for improvement in the low-temperature performance of nickel/metal hydride batteries. As the Fe-content in the alloy increases, the following was observed: lattice constant a first increases and then decreases; lattice constant c and c/a ratio increase; unit cell volume increases monotonically; the main AB_5 phase becomes hyper-stoichiometric containing no Zr and its Fe-content is close to the target composition; an additional AB_7 phase appears; maximum gaseous hydrogen storage, PCT plateau pressure, and hysteresis first increase and then decrease while the trend of reversible hydrogen storage is the opposite; enthalpy and entropy of hydride formation remain unchanged; electrochemical full capacity decreases while the high-rate dischargeability and surface reaction exchange current increase; and bulk hydrogen diffusion increases first and then decreases by very small amounts. The product of charge-transfer resistance and double-layer capacitance measured at −40 °C indicates an improvement in the surface catalysis with Fe-addition. In the sealed cell, the addition of Fe improves both the specific power and −10 °C low temperature performance, slightly reduces the charge retention, and first marginally improves and then deteriorates the cycle life performance.

1. Introduction

Most of the Fe-substitution in rare-earth based AB_5 metal hydride (MH) alloys are for the purpose of replacing expensive Co [1–17]. The general drawback of this approach is the resulting sacrifice in cycle life due to an increase in the pulverization rate during cycling. However, contradictory results of similar [18] or even improving cycle life [7,11,15,19] by partial substitution of Fe for Co have also been previously reported. Other features also cited include decreases in both anti-corrosion capability [9,20,21] and high-rate dischargeability (HRD) [6,8,22], an improvement [8,22] or hindrance [20] in activation, an easy formation of surface metallic clusters [23], and a lower hydrogen diffusion coefficient [5,6,11,21].

Besides the cost issue, Fe is an interesting substitution element in AB_5 MH alloys due to its atomic radius, number of electrons, and electronegativity being similar to those of Ni and Co. With an advantage of increasing surface area [24], Fe may be a candidate for low-temperature applications. Previous works of partially replacing Ni with Fe in AB_5 MH alloy showed both lower [25–27] and higher [28,29] gaseous hydrogen storages, either lower [25–27,30,31] or higher equilibrium plateau pressures [32], a low electrochemical capacity [24,33,34], a higher HRD due to higher surface area [24,34] or a lower HRD due to low exchange current and diffusion coefficient [35], and a harder activation [31,34]. In the case of Fe substitution for both Ni and Co, both the electrochemical capacity and plateau pressure decrease, and both lattice constants increase [36]. Since contradicting results of Fe-addition have been reported, a revisiting of the same subject is necessary. Recently, low-temperature performance has become the major barrier which prevents a nickel/metal hydride battery (Ni/MH) from replacing a NiCd battery. Cu was first introduced as a modifier element dedicated for −30 °C applications [37]. In this study, the effects of Fe-substitution for Ni into the structures and electrochemical properties of these low-temperature AB_5 MH alloys are investigated with a focus on improvement in Ni/MH battery performance, especially at low temperature.

2. Experimental setup

In this study, induction melting was performed under an argon atmosphere in a 2 kg furnace using a $MgAl_2O_4$ crucible, an alumina tundish, and a steel pancake-shape mold. The ingots were annealed in vacuum (1×10^{-8} Torr) at 960 °C for 10 h before being mechanically crushed into −200 mesh powder. The chemical

* Corresponding author. Tel.: +1 248 293 7000; fax: +1 248 299 4520.
E-mail addresses: kyoung@ovonic.com, kwoyoung@yahoo.com (K. Young).

0925-8388/$ – see front matter © 2011 Elsevier B.V. All rights reserved.
doi:10.1016/j.jallcom.2011.04.102

composition of each sample was examined by a Varian *Liberty* 100 inductively coupled plasma (ICP) system. A Philips *X'Pert Pro* X-ray diffractometer (XRD) was used to study the microstructure, and a JOEL-*JSM6320F* scanning electron microscope (SEM) with energy dispersive spectroscopy (EDS) capability was used to study the phase distribution and composition. PCT characteristics for each sample were measured using a Suzuki–Shokan multi-channel PCT system. In the PCT analysis, each sample was first activated by performing 4 room temperature absorption/desorption cycles; then, PCT isotherms at 30, 45, and 60 °C were measured. Details of both electrode and cell preparations as well as measurement methods have been reported previously [38,39]. The hydrogen diffusion and surface charge-transfer current measurements were performed using an Arbin Instruments BT4+ Portable Battery Test System. AC impedance measurements were conducted using a Solartron 1250 Frequency Response Analyzer with sine wave of amplitude 10 mV and frequency range of 10 mHz–10 kHz. Prior to the measurements, the electrodes were subjected to one full charge/discharge cycle at a C/10 rate using a Solartron 1470 Cell Test galvanostat, recharged to 100% state-of-charge (SOC), subsequently discharged to 80% (SOC), and then finally cooled to −40 °C.

3. Results and discussion

Four alloys with Fe substituting for Ni, $La_{10.5}Ce_{4.3}Pr_{0.5}Nd_{1.4}Ni_{64.3-x}Co_{5.0}Mn_{4.6}Al_{6.0}Cu_{3.2}Zr_{0.2}Fe_x$ (x = 0.0, 0.5, 1.0, and 1.5), were prepared by induction melting, and their design compositions are listed in Table 1. Fe0 alloy, the same base alloy used in a Mo-substitution study [40], is a derivative of a La-rich misch-metal based AB_5 alloy which has a good low-temperature performance at −30 °C [41]. In Fe0 alloy, Cu was added in order to engineer the shape of metallic inclusions and to create tunnels in the surface oxide interfaces [37]. Zr is included as a compensation for the reduced amount of Co used in the alloy [42] in order to increase the cycle life. The ICP results of all four alloys, as listed in Table 1, are very close to the design compositions. Small amount of La went into the slag and was removed by the tundish installed between the crucible pouring spout and the mold.

3.1. XRD structure analysis

The XRD spectra of four alloys in this study after annealing are shown in Fig. 1. Annealing is necessary in misch-metal based AB_5 MH alloys to ensure better uniformity and to extend the cycle life [43,44]. All peaks are from reflections of a $CaCu_5$ crystal structure. As the Fe-content increases, the (1 0 3) peak intensity increases from almost zero to about one half that of the (2 2 0) peak. There are various (1 0 3)/(2 2 0) peak ratios reported in the AB_5 systems: almost zero for unannealed $Mm(NiCoMnAl)_5$ [45] and 3-h annealed $Mm(NiCoMnAl)_5$ [46]; about one quarter from $LaNi_5$ [47,48], 6-h annealed low-Co AB_5 [49], and unannealed $AB_{4.9}$ [50]; one third from a low-Co $AB_{4.9}$ alloy [9] and $MmNi_5$ [51]; one half from a 8-h annealed $Mm(NiCoMnAl)_5$[52] and a 3-h annealed $Mm(NiCoMnAl)_5Li_{0.103}$ alloy [46]; and higher than 1 in a low-Co $AB_{5.4}$ alloy [53]. In a series of $La(NiAlCoMn)_5V_x$ alloys, the (1 0 3)/(2 2 0) peak ratio increases with increasing V-contents [54]. In our case, Fe may occupy a particular B-site (3 g) and alter the form factor of the (1 0 3) peak after annealing as was the case of $LaNi_{5-x}Fe_x$ studied by Mössbauer measurement [55]. In the current study, the (1 0 3)/(2 2 0) peaks ratio from un-annealed samples were much smaller than those reported previously.

Lattice constants a, c, c/a ratio, and the unit cell volume for each alloy are listed in Table 2. As the Fe-content in the alloy increases, the a value first increases and then decreases slightly while the c value increases monotonically. As a result, the c/a ratio, strongly

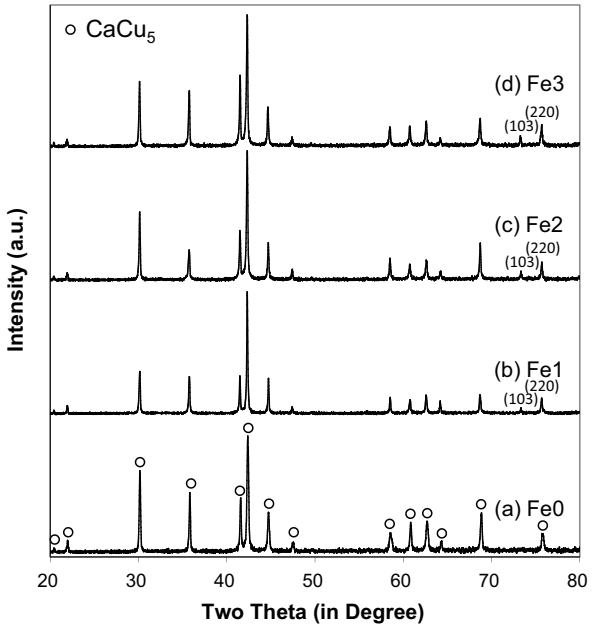

Fig. 1. XRD spectra using Cu K_α as the radiation source for alloys Fe0 (a), Fe1 (b), Fe2 (c), and Fe3 (d). Only reflections from a $CaCu_5$ crystal structure are present.

linked to the cycling pulverization rate [56], first it decreases and then increases with the increasing Fe-content. Lattice parameter a together with a few more properties described in later sections are affected by two driving forces with opposite directions. The larger atomic size of Fe increases the lattice constant a, but the formation of A-site Ni-dumbbell [57] reduces it. This may be related to the contradictory results from Fe-substitution found in the literatures. The $CaCu_5$ unit cell volume calculated from the lattice constants increases with the Fe-content. The increase in unit cell volume implies Fe-containing alloys have stronger metal–hydrogen bond strength and consequently a lower equilibrium plateau pressure. The crystallite sizes estimated from the full-width at half maximum (FWHM) of the $CaCu_5$ (0 0 1) diffraction peak are also listed in Table 2. The crystallite size increases first and then decreases as the Fe-content in the alloy increases.

3.2. SEM/EDS phase analysis

The microstructures for this series of alloys were studied by SEM. SEM back-scattering electron images (BEI) from alloys Fe1, Fe2, and Fe3 are presented in Fig. 2. The compositions in several areas identified numerically in the micrographs were studied by EDS and the results are listed in Table 3. The microstructure of the Fe-free Fe0 was shown in a previous publication (Fig. 3a in Ref. [38]) and can be summarized as: main AB_5 phase with occasional La–Ce metal inclusions and a $ZrNi_5$ secondary phase. The La–Ce inclusion contains a much higher level of Zr than the main working phase does and therefore can reduce the $ZrNi_5$ phase abundance. In the Fe-containing alloys, the location of Zr shifts from La and La_2Ni_3 (Fe1), to La_2Ni_3, ZrNi, and ZrO_2 (Fe2), and finally ZrO_2 (Fe3) as the Fe-content increases. There is no detectable Zr in the main AB_5 phase and therefore the predicted advantage of adding Zr to enhance the cycle life is not obtained. Due to the formation of La-rich phases, such as La-inclusion and La_2Ni_3, the main AB_5 phase becomes hyper-stoichiometric (B/A ratio of about 6.4) which is poor in La. The hyper-stoichiometry is good for cycle life as it results in the formation of Ni-dumbbell pairs in the A-site [57]. Unlike the case of Mo substitution, Fe was successfully doped into the main phase at a percentage slightly lower than the target value.

Table 1
Comparison of design composition and ICP result.

		La	Ce	Pr	Nd	Ni	Co	Mn	Al	Cu	Zr	Fe
Fe0	Design	10.5	4.3	0.5	1.4	64.3	5.0	4.6	6.0	3.2	0.2	0.0
	ICP	10.4	4.3	0.4	1.3	64.7	5.3	4.4	5.7	3.3	0.2	0.0
Fe1	Design	10.5	4.3	0.5	1.4	63.8	5.0	4.6	6.0	3.2	0.2	0.5
	ICP	9.8	4.1	0.5	1.4	64.9	4.9	4.6	5.9	3.3	0.2	0.5
Fe2	Design	10.5	4.3	0.5	1.4	63.3	5.0	4.6	6.0	3.2	0.2	1.0
	ICP	10.0	4.1	0.5	1.4	63.8	4.9	4.7	6.0	3.3	0.2	1.1
Fe3	Design	10.5	4.3	0.5	1.4	62.8	5.0	4.6	6.0	3.2	0.2	1.5
	ICP	9.8	4.2	0.5	1.3	63.7	4.9	4.6	6.1	3.2	0.2	1.5

Table 2
Lattice constants a and c, a/c ratio, $CaCu_5$ lattice volume, full width at half maximum (2θ, in degrees) for (1 0 3) reflection peak, and corresponding crystallite size from XRD analysis.

Alloy #	a (in Å)	c (in Å)	c/a	V_{CaCu5} (in Å^3)	FWHM (0 0 1)	Crystallite size (in Å)
Fe0	5.011	4.048	0.8078	88.03	0.169	826
Fe1	5.020	4.049	0.8066	88.37	0.133	>1000
Fe2	5.020	4.050	0.8068	88.39	0.145	>1000
Fe3	5.018	4.054	0.8079	88.40	0.176	756

At higher Fe-contents, higher stoichiometry phases, such as AB_7, start to appear.

3.3. Gaseous study

Gaseous hydrogen storage properties of the alloys were studied by PCT. The resulting absorption and desorption isotherms measured at 30 °C and 45 °C for alloys Fe1–Fe3 are shown in Fig. 3a and b, respectively. The information obtained from the PCT study is summarized in Table 4. The plateau pressure increases slightly and then decreases. The initial increase is due to the hyper-stoichiometry in the main AB_5 phase and the latter decrease is from the expanding unit cell volume due to Fe-addition. The slope factor (SF) is defined as the ratio of the storage capacity between 0.01 and 0.5 MPa hydrogen pressure to the total capacity. The SF of each alloy is listed in Table 4 and can be used to determine the degree of disorder in the alloy [58,59]. As the Fe-content increases, the SF first remains about the same and then decreases slightly. The relatively higher SF in Fe2 may be related to the smaller crystallite found in XRD analysis. The hysteresis of the PCT isotherm, listed in Table 4, is defined as $\ln(P_a/P_d)$, where P_a and P_d are the absorption and desorption equilibrium pressures at 0.6 wt.%, respectively. Similar to Mo in AB_5, the hysteresis first increases and then decreases to the original value as the Fe-content increases. The initial increase in PCT hysteresis is due to the reduction of Zr-content in the main phase due to the formation of other Zr-rich secondary phases. The latter reduction is due to the formation of hyper-stoichiometry AB_7 phase. The trend of PCT hysteresis evolution follows that of the c/a ratio.

With increasing Fe-content, the maximum storage capacity first increases and then decreases. The increase is due to the larger unit cell resulting from Fe-addition and the decrease is due to formation of hyper-stoichiometry AB_7 phase with less hydrogen storage capability. The reversible capacity has the opposite trend. The addition of a small amount of Fe increases the unit cell and the storage capacity; it also increases the metal–hydrogen bond strength and makes it more difficult to release hydrogen. In the case of alloys with higher Fe-content, the hyper-stoichiometry AB_7 can release hydrogen more easily.

Desorption equilibrium pressures at 0.6 wt.% storage capacity measured at 30, 45, and 60 °C were used to calculate the changes in enthalpy (ΔH) and entropy (ΔS) by the equation

$$\Delta G = \Delta H - T\Delta S = RT \ln P \quad (1)$$

where R is the ideal gas constant and T is the absolute temperature. The results of these calculations are listed in Table 4. The variations in heat of hydride formations are small but still can be correlated

Table 3
EDS result in atomic percentages from area identified in SEM micrograph (Fig. 2). All numbers are in atomic percentages.

	La	Ce	Pr	Nd	Ni	Co	Mn	Al	Cu %	Zr	Fe	B/A Ratio	Phase
Fe1–1	70.5	9.8	0.0	2.7	9.7	0.2	0.0	1.4	1.0	4.6	0.0	0.2	La
Fe1–2	28.5	7.9	0.0	0.7	37	12.8	0.8	0.0	0.3	12.0	0.0	1.7	La_2Ni_3
Fe1–3	**8.2**	**4.5**	**0.0**	**0.9**	**65.6**	**4.7**	**4.5**	**8.0**	**3.4**	**0.0**	**0.3**	**6.4**	**AB_5**
Fe1–4	8.3	4.6	0.0	0.9	67.6	4.7	4.8	5.8	3.1	0.0	0.3	6.3	AB_5
Fe1–5	8.1	4.4	0.0	1.0	68.5	4.8	4.6	5.0	3.3	0.0	0.4	6.4	AB_5
Fe2–1	36.4	8.4	0.0	0.8	44.2	5.4	2.2	0.0	1.6	0.3	0.5	1.2	$LaNi/La_2Ni_3$
Fe2–2	27.6	6.9	0.0	0.4	49.3	9.4	2.4	0.4	1.4	1.4	0.8	1.9	La_2Ni_3
Fe2–3	40.2	7.9	1.1	1.0	40.9	3.2	2.5	0.0	2.5	0.2	0.5	1.0	LaNi
Fe2–4	**8.3**	**4.6**	**0.0**	**0.9**	**69.5**	**2.9**	**4.7**	**4.8**	**3.5**	**0.0**	**0.9**	**6.3**	**AB_5**
Fe2–5	6.6	4.1	0.3	1.0	44	1.8	3.7	3.7	2.7	31.3	0.8	7.3	ZrNi
Fe2–6	8.5	4.6	0.0	0.9	69.4	2.6	4.6	5.3	3.1	0.0	1.0	6.1	AB_5
Fe2–7	8.4	4.6	0.0	1.0	69.6	2.6	4.7	5.0	3.3	0.0	0.8	6.1	AB_5
Fe2–8	3.4	1.2	0.0	0.0	6.4	0.0	0.4	0.2	0.3	88	0.0	20.7	ZrO_2
Fe2–9	7.6	4.1	0.0	0.8	63.7	2.5	4.2	13.2	3.0	0.0	0.9	7.0	AB_7
Fe3–1	33.3	7.2	0.0	1.3	39.5	16.8	0.6	0.0	0.2	0.3	0.8	1.4	La_2Ni_3
Fe3–2	**8.2**	**4.5**	**0.0**	**0.9**	**68**	**4.6**	**4.4**	**4.9**	**3.2**	**0.0**	**1.3**	**6.4**	**AB_5**
Fe3–3	8.3	4.5	0.0	0.9	66.2	4.6	5.0	6.3	3.0	0.1	1.3	6.3	AB_5
Fe3–4	0.8	0.2	0.0	0.0	3.0	0.0	0.1	0.6	0.1	95.1	0.1	99.0	ZrO_2
Fe3–5	7.2	3.8	0.0	0.8	57.4	3.8	3.9	19.3	2.8	0.0	1.0	7.5	AB_7

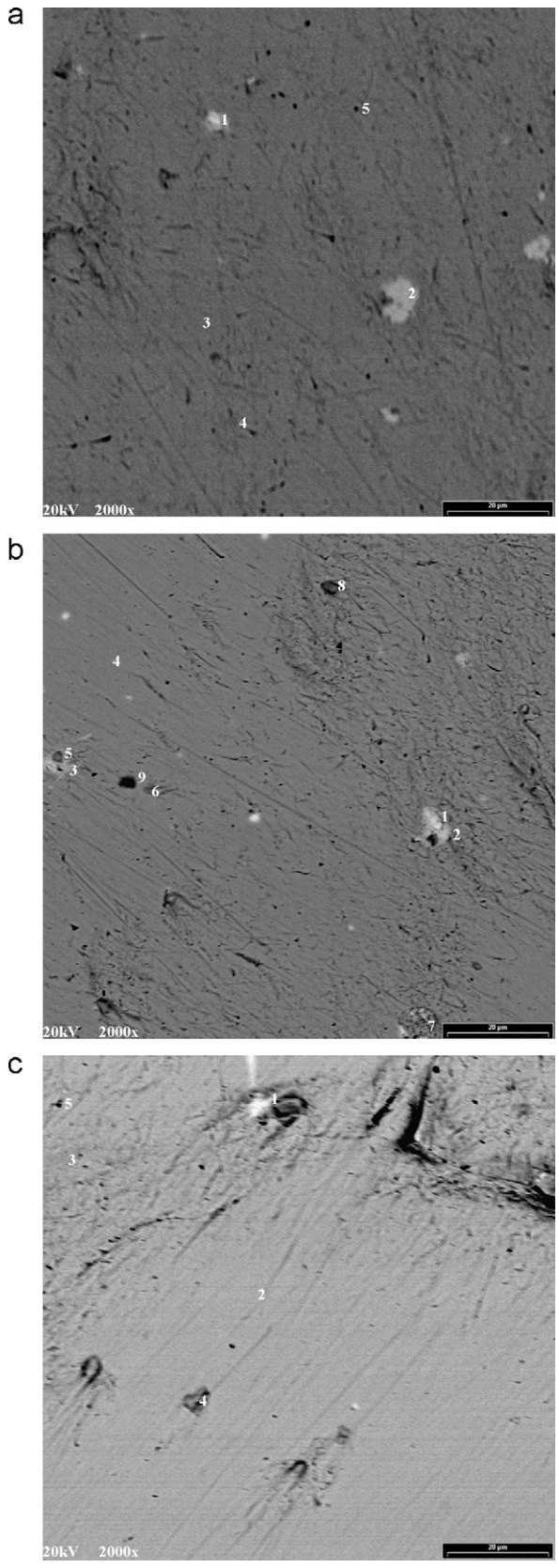

Fig. 2. SEM backscattering images for after annealed alloys Fe1 (a), Fe2 (b), and Fe3 (c).

Table 4
Summary of chemical composition (in atomic percentage), gas phase properties (plateau pressure, slope factor, hysteresis, and maximum capacity), and results from half-cell measurement (pre-charge, capacity, and high-rate dischargeability) and full-cell (cycle life, charge retention, specific power, and low-temperature performance) measurement.

	Des. pressure at 0.6%, at 30 °C (MPa)	Slope factor at 30 °C	PCT hysteresis at 0.6%, 30 °C	Max. cap. at 30 °C (wt.%)	Reversible cap. at 30 °C (wt.%)	$-\Delta H$ (kJ/mol)	$-\Delta S$ (J/mol K)	Pre-charge (mAh/g)	Cap. at 100 mA/g (mAh/g)	Cap. at 12 mA/g (mAh/g)	HRD	Diffusion coefficient (10^{-10} cm^2/s)	Exchange current (mA/g)	Charge transfer resistance at −40 °C (Ω g)	Double-layer capacitance at −40 °C (Farad/g)	70% cycle life	30 days charge retention (%)	Room temp. specific power (W/kg)	Low-temp. −10 °C, 0.5 C (%)
Fe0	0.018	0.86	0.13	1.26	1.21	39.9	117	0	311	333	0.934	10.9	33.1	5.4	1.02	135	76	179	89
Fe1	0.019	0.88	0.20	1.30	1.10	40.9	119	0	296	313	0.948	11.5	33.7	3.3	1.49	145	64	196	96
Fe2	0.013	0.87	0.16	1.30	1.03	40.3	116	0	300	312	0.963	9.6	50.0	4.9	1.05	35	65	195	93
Fe3	0.012	0.83	0.12	1.25	1.13	40.1	115	1	311	314	0.989	9.6	48.0	3.5	1.07	40	65	197	94

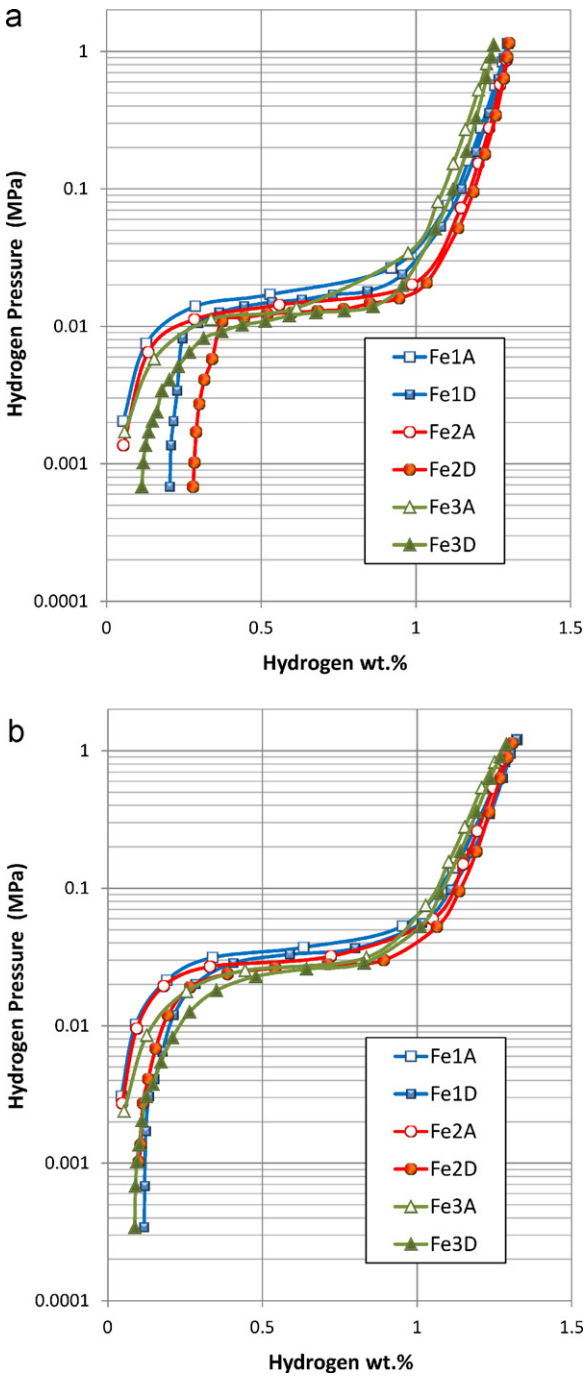

Fig. 3. 30 °C (a) and 45 °C (b) PCT isotherms of alloys Fe1, Fe2, and Fe3. Open and solid symbols are for absorption and desorption curves, respectively.

to the maximum capacity as proposed by Ma et al. [60]. The driving forces from large unit cell and hyper-stoichiometry must be about the same, and therefore the net change resulting from Fe-addition is small. The ΔS values are very similar and close to the ΔS between the hydrogen gas and hydrogen in the solid [61,31], implying a complete ordered β hydride phase.

3.4. Electrochemical measurement

Discharge capacities of the four alloys were measured in a flooded cell against a partially pre-charged $Ni(OH)_2$ as the positive electrode. Unlike AB_2 alloys, pre-activation in a hot alkaline solution was not performed. The cell was first discharged with a

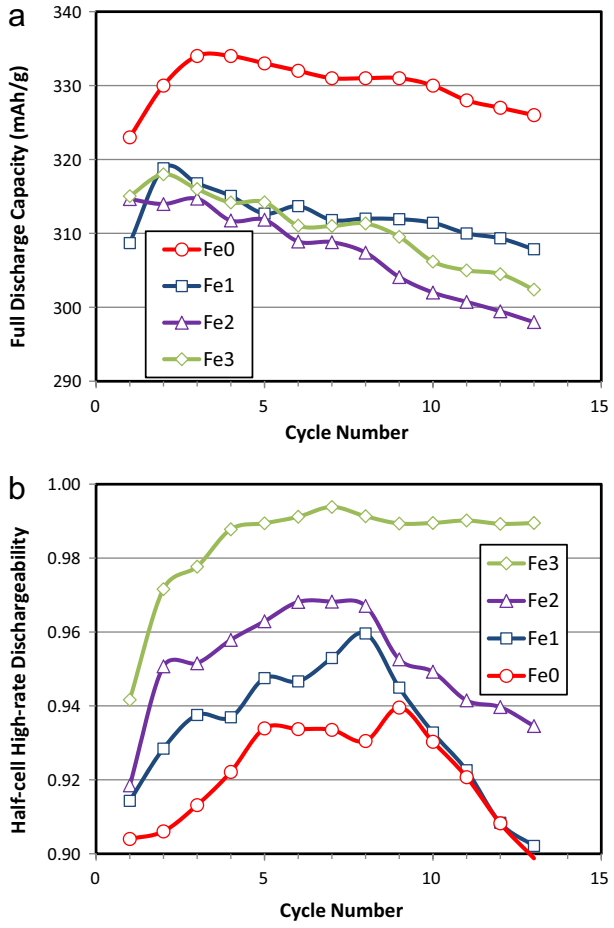

Fig. 4. The full discharge capacity measured at 12 mA/g (a) and half-cell HRD as defined as the ratio between capacities measured at 100 and 12 mA/g for the first 13 cycles.

small current density at 5 mA/g. The initial discharge capacity prior to any charge input is due to the hydrogen absorption generated as a result of the metal oxidation in the electrolyte, and it can be used to quantify the ease of activation [62]. A higher initial discharge capacity can be correlated to easier oxidation/activation of the alloy. The amount of pre-charge in mAh/g for each alloy is listed in Table 4. With a relative stability in KOH solution [63], Fe-addition does not change the formation process significantly, which is in agreement with prior literature [64] and very different from the case of Mo-substitution.

The full discharge capacities of the first 13 cycles measured with a current of 12 mA/g are plotted in Fig. 4a. The discharge capacities of the Fe-containing alloys are similar and are lower than that from Fe-free alloy, which is consistent with the reversible gaseous hydrogen storage capacities found from the PCT analysis. The half-cell HRD of each alloy, defined as the ratio of discharge capacity measured at 100 mA/g to that at 12 mA/g, is plotted in Fig. 4b. Numbers obtained from the 5th cycle are listed in Table 4. The half-cell HRD improves with the increase in Fe-content.

Both the bulk diffusion coefficient (D) and the surface exchange current (I_o) are important parameters for analysing the MH alloy to be used in a sealed Ni/MH battery. The details of both measurements were previously reported [65], and the values are listed in Table 4. While the D values for all alloys are similar (with a small increase in Fe1 and decreases in Fe2 and Fe3), the I_o values of the Fe-containing alloys are considerably higher than those in the Fe-free alloy. Therefore, the increase in the half-cell HRD is mainly due to the improvement of the surface reaction and is not related to the

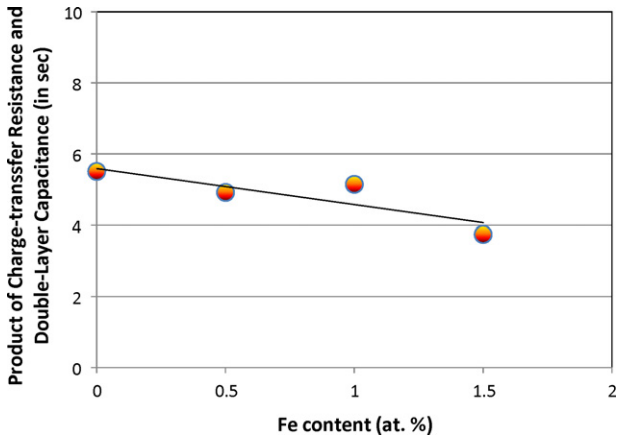

Fig. 5. The product of charge-transfer resistance and double-layer capacitance measured at −40 °C as a function of Fe-content in the alloy.

bulk diffusion of hydrogen. In a Fe-containing AB_2 MH alloy, an Fe-rich surface is formed after activation and is believed to contribute positively to the surface reaction [66].

The low-temperature characteristic of these alloys was further studied using AC impedance measurement conducted at −40 °C. At temperatures as low as −40 °C, the surface charge-transfer reaction on the negative electrode becomes more dominating in the discharge kinetics [67]. The charge-transfer resistance (R) and double-layer capacitance (C) were calculated from the Cole–Cole plot and are listed in Table 4. All the Fe-containing alloys show lower R values than the Fe-free Fe0 alloy. Only Fe1 shows a relatively larger C value compared to those of the other alloys, indicating a small amount of Fe (0.5%) is useful to increase the reaction area. The product of charge-transfer resistance and double-layer capacitance measured at −40 °C as a function of Fe-content in the alloy is plotted against the Fe-content in Fig. 5. It clearly shows the advantage in using Fe to increase the surface catalytic activity. The slope of the trend line in Fig. 5 is twice that of a similar curve with Mo-addition [38] (Fig. 7 in Ref. [38]). Therefore, Fe is more effective in catalysing the surface reaction at low temperature than Mo when same amount is added in the alloy formula.

Four important Ni/MH technical parameters (cycle life, charge retention, specific power, and low-temperature performance) for the MH electrode made from each alloy are listed in Table 4. The cycle life performance (measured by the number of cycles reaching 70% of the original capacity) of Fe1 is similar to the base alloy Fe0. Higher Fe-contents degrades the cycle life; this may be due to the introduction of hyper-stoichiometric AB_7 phase which has a different amount of expansion during the hydride/dehydride cycling and contributes to an early failure of electrode due to disintegration.

The 30-day charge retention values are listed in Table 4. Charge retention of the Fe-containing alloys is slightly worse than the Fe-free base alloy, as the Fe dissolves into the electrolyte during cycling [66,68]. The multi-valence property of the Fe-ion may contribute to the oxidation–reduction shuttling effect between the positive and negative electrodes thus lowering charge retention. The specific power measured at room temperature is also listed in Table 4. The powers of Fe-containing alloys are comparable and higher than the Fe-free Fe0 alloy, which is consistent with the half-cell HRD results.

Low-temperature performance, defined as the ratio of the capacity measured at 0.5 C rate and −10 °C to the capacity measured at the same rate and room temperature, is listed in Table 4 for each of the alloys. Again, the Fe-containing alloys show better −10 °C dischargeability than the Fe-free alloy. Fe further improves the low-temperature performance of alloys designed for better low-temperature power capability.

4. Conclusions

The Fe addition to an AB_5 alloy previously designed for −30 °C low-temperature performance shows improvements in room temperature power, −10 °C full-cell, and −40 °C half-cell measurement due to an increase in the surface catalytic ability. Taking into consideration the balancing of low temperature performance with the general battery performance, especially cycle life, a Fe-content at 0.5 at.% is recommended.

References

[1] J.M. Cocciantelli, P. Bernard, S. Fernandez, J. Atkin, J. Alloys Compd. 253–254 (1997) 642.
[2] F. Lichtenberg, U. Köhler, A. Fölzer, N.J.E. Adkins, A. Züttel, J. Alloys Compd. 253–254 (1997) 570.
[3] W. Hu, J. Alloys Compd. 289 (1999) 299.
[4] C. Iwakura, K. Ohkawa, H. Senoh, H. Inoue, Electrochim. Acta 46 (2001) 4383.
[5] C. Khaldi, H. Mathlouthi, J. Lamloumi, A. Percheron-Guégan, Int. J. Hydrogen Energy 29 (2004) 307.
[6] X. Chen, Y. Lei, B. Liao, F. Wei, L. Chen, Chin. J. Nonferrous Metals 14 (2004) 1862.
[7] X. Zhu, Y. Zhou, F. Chong, X. Li, W. Pan, J. Rare Earths 22 (2004) 245.
[8] Y. Zhou, X. Zhu, Science & Technology of Baotou Steel (Group) Corporation V. 31, No. 2, (April, 2005) 35. doi:cnki:ISSN:1009-5438.0.2005-02-015.
[9] Y. Zhang, G. Wang, X. Dong, S. Guo, J. Ren, X. Wang, J. Power Sources 148 (2005) 105.
[10] Y. Zhang, X. Dong, G. Wang, S. Guo, X. Wang, J. Power Sources 140 (2005) 381.
[11] Y. Zhao, Y. Zhang, G. Wang, X. Dong, S. Guo, X. Wang, J. Alloys Compd. 388 (2005) 284.
[12] M. Tliha, H. Mathlouthi, C. Khaldi, J. Lamloumi, A. Percheron-Guégan, J. Power Sources 160 (2006) 1391.
[13] M.B. Moussa, M. Abedellaoui, H. Mathlouthi, J. Lamloumi, A. Percheron-Guégan, J. Alloys Compd. 407 (2006) 256.
[14] M. Ayari, V. Paul-Boncour, J. Lamloumi, H. Mathlouthi, A. Percheron-Guégan, J. Alloys Compd. 420 (2006) 251.
[15] M.B. Moussa, M. Abdellaoui, H. Mathlouthi, J. Lamloumi, A. Percheron-Guégan, J. Alloys Compd. 458 (2008) 410.
[16] M. Tliha, S. Boussami, H. Mathlouthi, J. Lamloumi, A. Percheron-Guégan, J. Alloys Compd. 506 (2010) 559.
[17] M. Tliha, S. Boussami, H. Mathlouthi, J. Lamloumi, A. Percheron-Guégan, Mat. Sci. Eng. B 175 (2010) 60.
[18] S. Vivet, J.M. Joubert, B. Knosp, A. Percheron-Guégan, J. Alloys Compd. 356–357 (2003) 779.
[19] A. Züttle, D. Chartouni, K. Gross, P. Spatz, M. Bächler, F. Lichtenberg, A. Fölzer, N.J.E. Adkins, J. Alloys Compd. 253–254 (1997) 626.
[20] C. Khaldi, H. Mathlouthi, J. Lamloumi, A. Percheron-Guégan, J. Alloys Compd. 360 (2003) 266.
[21] C. Khaldi, H. Mathlouthi, J. Lamloumi, A. Percheron-Guégan, J. Alloys Compd. 384 (2004) 249.
[22] L. Chen, Rare Met. Mater. Eng. 28 (1999) 302.
[23] M. Ayari, V. Paul-Boncour, J. Lamloumi, A. Percheron-Guégan, J. Magn. Magn. Mater. 242–245 (2002) 850.
[24] C. Iwakura, T. Oura, H. Inoue, M. Matsuoka, Electrochim. Acta 41 (1996) 117.
[25] H.H.V. Mal, K.H. Buschow, A.R. Miedema, J. Less Comm. Met. 35 (1974) 65.
[26] J. Lamloumi, A. Percheron-guegan, C. Lartigue, J.C. Achard, G. Jehanno, J. Less Comm. Met. 130 (1987) 111.
[27] F. Meli, A. Züttle, L. Schlapbach, J. Alloys Compd. 231 (1995) 639.
[28] R.K. Singh, B.K. Gupta, M.V. Lototsky, O.N. Srivastava, J. Alloys Compd. 373 (2004) 208.
[29] R.K. Singh, B.K. Gupta, M.V. Lototsky, O.N. Srivastava, Int. J. Hydrogen Energy 32 (2007) 2971.
[30] E.L. Huston, G.D. Sandrock, J. Less Comm. Met. 74 (1980) 4365.
[31] S.L. Li, P. Wang, W. Chen, G. Luo, D.M. Chen, K. Yang, J. Alloys Compd. 485 (2009) 867.
[32] K. Yang, X. Liu, C. Dai, in: T.N. Veziroglu, Y. Zhu, D. Bao (Eds.), Hydrogen Systems, vol. 1, Pergamon, NY, 1986, p. 383.
[33] L. Chen, Y. Lei, G. Zhu, Q. Wang, Rare Met. Mater. Eng. 27 (1998) 135.
[34] X. Wei, S. Liu, H. Dong, P. Zhang, Y. Liu, J. Zhu, G. Yu, Electrochim. Acta 52 (2007) 2423.
[35] H. Yang, Y. Chen, M. Tao, C. Wu, J. Shao, G. Deng, Electrochim. Acta 55 (2010) 648.
[36] E.A. Kumar, M.P. Maiya, S.S. Murthy, B. Viswanathan, J. Alloys Compd. 476 (2009) 92.
[37] M.A. Fetcenko, S.R. Ovshinsky, K. Young, B. Reichman, T. Ouchi, J. Koch, W. Mays, U.S. Patent 6,830,725 (2004).
[38] K. Young, M.A. Fetcenko, T. Ouchi, F. Li, J. Koch, J. Alloys Compd. 464 (2008) 238.
[39] K. Young, M.A. Fetcenko, J. Koch, K. Morii, T. Shimizu, J. Alloys Compd. 486 (2009) 559.
[40] K. Young, T. Ouchi, B. Reichman, J. Koch, M.A. Fetcenko, J. Alloys Compd. 509 (2011) 3995.
[41] K. Young, T. Ouchi, M.A. Fetcenko, U.S. Patent 7,344,677 B2 (2008).

[42] M.A. Fetcenko, K. Young, S.R. Ovshinsky, T. Ouchi, U.S. Patent 7,393,500 B2 (2008).
[43] G.D. Adzic, J.R. Johnson, J.J. Reilly, J. McBreen, S. Mukerjee, M.P.S. Kumar, W. Zhang, S. Srinivasan, J. Electrochem. Soc. 142 (1995) 3429.
[44] H. Kaiya, T. Ookawa, J. Alloys Compd. 231 (1995) 598.
[45] C. Seo, S. Choi, J. Choi, C. Park, P. Lee, J. Lee, Int. J. Hydrogen Energy 28 (2003) 317.
[46] L. Wang, H. Yuan, H. Yang, K. Zhou, D. Song, Y. Zhang, J. Alloys Compd. 302 (2000) 65.
[47] PDF# 00-050-0777 and PDF # 00-055-0277, published by International Centre for Diffraction Data, Newtown, PA (2011).
[48] Y. Li, Y. Cheng, M.A. Habib, J. Alloys Compd. 209 (1994) 7.
[49] W. Zhang, S. Han, J. Hao, Y. Li, T. Bai, J. Zhang, Electrochim. Acta 54 (2009) 1383.
[50] S. Yang, S. Han, Y. Li, S. Yang, L. Hu, Mater. Sci. Eng. B 176 (2011) 231.
[51] L.O. Valøen, A. Zaluska, L. Zaluski, H. Tanaka, N. Kuriyama, J.O. Ström-Olsen, R. Tunold, J. Alloys Compd. 306 (2000) 235.
[52] J. Ma, H. Pan, C. Chen, Q. Wang, Int. J. Hydrogen Energy 27 (2002) 57.
[53] R. Li, J. Wu, S. Zhu, J. Qian, J. Rare Earths 24 (2006) 341.
[54] C. Seo, S. Choi, J. Choi, C. Park, J. Lee, Int. J. Hydrogen Energy 28 (2003) 967.
[55] S.J. Campbell, R.K. Day, J.B. Dunlop, A.M. Stewart, J. Magn. Magn. Mater. 31–34 (1983) 167.
[56] Y. Osumi, H. Suzuki, A. Kato, K. Oguro, S. Kawai, M. Kaneko, J. Less Comm. Met 89 (1983) 287.
[57] P.H.L. Notten, R.E.F. Einerhand, J.L.C. Daams, J. Alloys Compd. 231 (1995) 604.
[58] K. Young, T. Ouchi, J. Koch, M.A. Fetcenko, J. Alloys Compd. 477 (2009) 749.
[59] K. Young, T. Ouchi, M.A. Fetcenko, R.K. Regmi, G. Lawes, J. Alloys Compd. 490 (2010) 282.
[60] X. Ma, X. Wei, H. Dong, Y. Liu, J. Alloys Compd. 490 (2010) 548.
[61] L. Schlapbach, A. Züttle, Nature 414 (2001) 353.
[62] C. Iwakura, W.K. Choi, S. Zhang, H. Inoue, Electrochim. Acta 44 (1998) 1677.
[63] M. Pourbaix, Atlas of Electrochemical Equilibria in Aqueous Solution, 2nd English ed., NACE, Houston, Texas, USA, 1974, p. 313.
[64] Q. Zhang, G. Li, C. Zhou, R. Wang, Battery Bimonthly 28 (1998) 208.
[65] F. Li, K. Young, T. Ouchi, M.A. Fetcenko, J. Alloys Compd. 471 (2009) 371.
[66] M.Y. Song, I.H. Kwon, D.S. Ahn, M.S. Sohn, Met. Mater. Int. 7 (2001) 257.
[67] H. Senoh, Y. Hara, H. Inoue, C. Iwakura, Electrochim. Acta 46 (2001) 967.
[68] M.Y. Song, D. Ahn, I.H. Kwon, S.J. Chough, J. Electrochem. Soc. 148 (2001) A1041.